TITLE

Two-Minute Quantitative Susceptibility Mapping from Three-dimensional Echo-planar Imaging: Accuracy, Reliability, and Detection Performance in Patients with Cerebral Microbleeds

ABSTRACT

Objectives

To assess the accuracy, reliability, and cerebral microbleeds (CMB) detection performance of 2-min quantitative susceptibility mapping (QSM) from 3-dimensional echo-planar imaging (3D-EPI).

Materials and Methods

Gadolinium phantom study was conducted using 3D-EPI, single-TE, and multi-TE gradient-recalled echo (GRE) sequences on two 3-T MR scanners to assess the accuracy between measured and theoretical susceptibility values. The institutional review board approved this prospective study, and 40 healthy volunteers were enrolled with written consent between April 2018 and October 2019. Each underwent 3D-EPI, single-TE, and multi-TE GRE sequences consecutively on one 3-T MR scanner, and QSMs were calculated to assess the reliability of 3D-EPI QSM. Intraclass correlation coefficient (ICC), linear regression, and Bland-Altman plots were calculated. Patients with CMB who underwent both 3D-EPI and GRE QSM scans were retrospectively enrolled. Two radiologists evaluated images independently, and Cohen κ coefficients were calculated to compare CMB detection performance.

Results

Phantom study showed excellent validity of 3D-EPI QSM on both MR scanners: Skyra, R^2 = 0.996, P < 0.001, ICC = 0.997, mean difference -2 ppb (95%CI -45 to 40 ppb); Prisma, R^2 = 0.992, P < 0.001, ICC = 0.988, mean difference 15 ppb (95%CI -67 to 97 ppb). Human study of 40 healthy volunteers (59 ± 13 years, 25 women) showed excellent reliability with 3D-EPI QSM for both single-TE and multi-TE GRE (R^2 = 0.981, P < 0.001, ICC = 0.988; R^2 = 0.983, P < 0.001, ICC = 0.990, respectively), supported by a Bland-

Altman mean difference of 4 ppb (95%CI -15 to 23 ppb) for single-TE GRE, and 3 ppb (95%CI -15 to 20 ppb) for multi-TE GRE. CMB detection performance evaluation from 38 patients (51 ± 20 years, 20 women) showed almost perfect agreement between 3D-EPI and GRE QSM for both raters (κ = 0.923 and 0.942, P < 0.001).

Conclusions

Faster QSM from 3D-EPI demonstrated excellent accuracy, reliability, and cerebral microbleeds detection performance.

Key Words

3D-EPI; QSM; Accuracy; Reliability; Microbleeds; MRI

Introduction

Quantitative susceptibility mapping (QSM) is an MRI post-processing technique to quantitatively estimate local magnetic susceptibility in biologic tissue. QSM is commonly derived from gradient-recalled echo (GRE)-phase measurement through the deconvolution process to reveal local tissue magnetic susceptibility. The magnetic susceptibility of brain tissue has been studied with QSM by focusing on iron, myelin, calcification,[1] and gadolinium deposition.[2] The relationship with CT attenuation has also been studied, revealing a positive correlation in the globus pallidus and hemorrhagic lesions and negative correlation in the choroid plexus and calcified lesions.[3] Various applications of QSM have been studied, including evaluating abnormal iron accumulation in specific brain regions for Alzheimer's disease,[4] multiple sclerosis,[5] and Parkinson's disease.[6] In addition, QSM has proven useful in evaluating cerebral microbleeds (CMB),[7] with notable consistency in measuring CMB burden, and differentiating between hemorrhage and calcification,[8] which showed better sensitivity and specificity than SWI phase imaging.

However, QSM is still rarely used in routine MR examinations, even though QSM is clinically useful for CMB detection. QSM requires a relatively long acquisition time sequence, and the typical QSM scan using the GRE sequence takes around 5 min for a 1-mm isotropic resolution. Apart from decreasing patient flow efficiency and incurring a higher probability of motion artifacts, some patients (such as those with severe disease burden) cannot tolerate long MR scan times.

Echo-planar imaging (EPI) facilitates faster acquisition by acquiring multiple lines of imaging data after a single radiofrequency (RF) excitation. QSM derived from 3D-EPI achieves a clinically feasible shorter scan time,[9] at around 2 min in our institution. Even though this is longer than 2D-EPI acquisition, which is typically less than half a minute,[10, 11]

3D-EPI improves both spatial resolution and signal-to-noise ratio (SNR),[12] thus reduces the partial volume effects in CMB detection. The accuracy, reliability, and CMB detection performance of 3D-EPI QSM have yet to be thoroughly investigated. Few past studies have comprised all of the phantom, healthy volunteers, and clinical patients' study at once. The purpose of this study was thus to assess the accuracy, reliability, and CMB detection performance of 3D-EPI QSM, compared with GRE QSM.

Materials and Methods

The institutional review board approved this prospective study for healthy volunteers, and written informed consent was obtained from all participants prior to enrollment. The institutional review board also approved the retrospective observational study of patients, and the need to obtain written informed consent in those cases was waived.

Phantom

A phantom was constructed from 7 latex balloons, affixed and submerged in a cuboid plastic container filled with water. Each balloon contained 0.5 cm^3 of gadoterate meglumine solution (Magnescope; Guerbet, Villepinte, France) in concentrations of 0.25, 0.5, 0.75, 1.0, 1.5, 2.0 or 2.5 mmol/L, corresponding to theoretical susceptibility values of 0.0815, 0.163, 0.2445, 0.326, 0.489, 0.652 and 0.815 ppm, respectively.[13]

Healthy Volunteers and Patients

From April 2018 to October 2019, a total of 40 healthy volunteers with no known neurological disease were recruited to participate in this study. We also retrospectively

collected 672 consecutive patients who underwent 3D-EPI QSM scans in our hospital during that period. Among them, only patients with CMB were included. Subsequently, patients without corresponding GRE QSM or with a >1-year interval to the corresponding GRE QSM were excluded.

Image Acquisition

We conducted a phantom study using a 3-T MRI (MAGNETOM Skyra; Siemens Healthineers, Erlangen, Germany) with a 32-channel head coil, and another 3-T MRI (MAGNETOM Prisma; Siemens Healthineers) with a 64-channel head/neck coil. Meanwhile, we conducted a healthy volunteer study on a 3-T MRI (MAGNETOM Skyra) with a 32-channel head coil. Three consecutive imaging sequences for QSM were obtained in the same session: 3D-EPI (repetition time (TR), 57 ms; echo time (TE), 20 ms; flip angle (FA), 12°; field of view (FOV), 208 × 208 mm; matrix size, 208 × 208; echo train length (ETL), 15; 176 slices; parallel imaging factor, N/A; voxel size, 1 × 1 × 1 mm; slices resolution, 90%), single-TE GRE (TR, 28 ms; TE, 20 ms; FA, 15°; FOV, 180 × 230 mm; matrix size, 250 × 320; ETL, 1; 128 slices; parallel imaging factor, 2; voxel size, 0.72 × 0.72 × 1 mm, slices resolution, 90%), and multi-TE GRE (TR, 44 ms; TE, 3.6/9.5/15.4/21.3/27.2/33.1/39 ms; FA, 15°; FOV, 240 × 240 mm; matrix size, 256 × 256; ETL, 7; 128 slices; parallel imaging factor, 2; voxel size, 0.94 × 0.94 × 1 mm; slices resolution, 90%). Scan time was 1 minute 57 seconds for 3D-EPI, 4 minutes 44 seconds for single-TE GRE, and 5 minutes 1 second for multi-TE GRE. The T1 weighted images were also acquired for human study by using Three Dimensional Magnetization Prepared Rapid Acquisition GRE (3D-MPRAGE) sequence with the following parameters: TR, 1900 ms; TE, 2.6 ms; TI, 900 ms; FA, 9°; FOV, 230 × 230 mm; matrix size, 256 × 256; 256

slices; slice thickness, 0.9 mm; parallel imaging factor, 2; scan time, 4 minutes 23 seconds. Patients with CMB were scanned on either the 3-T MAGNETOM Skyra or Prisma with the corresponding coil, using 3D-EPI and single-TE GRE QSM.

QSM Reconstruction

Both the magnitude and phase data were saved for each 3D-EPI and GRE scan, and QSM was calculated from them using STI Suite version 3 (https://people.eecs.berkeley.edu/~chunlei.liu/software.html). Brain mask images were generated from magnitude images of 3D-EPI and GRE using the brain extraction tool (BET) of FMRIB software library (FSL) (https://fsl.fmrib.ox.ac.uk/fsl/fslwiki/BE). For phase unwrapping and background phase removal, we used the Laplacian-based phase unwrapping and variable-kernel sophisticated harmonic artifact reduction for phase data (V-SHARP) with kernel size up to 25 mm. Afterward, QSM was calculated from the local tissue phase map using the improved sparse linear equation and least-squares (iLSQR) algorithm. QSM reconstruction takes around 4 min on our workstation (Intel(R) Core(TM) i7-4770 CPU @ 3.40GHz, 32GB RAM). The QSM reconstruction process is outlined in Supplemental Digital Content 1 (Supplemental Figure 1).

Post-Imaging Processing

To analyze phantom data, circular region of interests (ROIs) were drawn semi-automatically at the center of the balloon using the ITK-SNAP application (www.itksnap.org), while a control ROI was placed in the surrounding water. Mean susceptibility values were measured using the built-in function of ITK-SNAP. In the healthy volunteer study, T1-weighted images were co-registered and segmented to create a

DARTEL template using SPM version 12 (https://www.fil.ion.ucl.ac.uk/spm/software/spm12/). The template was used for normalization and creating average QSM. Based on average QSM, VOIs were drawn semi-automatically using ITK-SNAP, comprising 12 paramagnetic VOIs (pairs of dentate nucleus, substantia nigra, red nucleus, putamen, globus pallidus, and caudate nucleus) and five diamagnetic VOIs (splenium of corpus callosum, pair of posterior limbs of internal capsule and parts of the optic radiation) (Fig. 1). ROIs of choroid plexus calcification were also created. Choroid plexus calcification was defined as a diamagnetic lesion inside the choroid plexus less than -0.06 ppm.[3] A board-certified radiologist (_._, with 8 years of neuroradiology experience) drew all ROIs/VOIs, which were then checked and confirmed by a senior radiologist (_._, with 22 years of neuroradiology experience). Size of VOIs and ROIs are provided in Supplemental Digital Content 2 (Supplemental Table 1a and 1b). VOIs were smoothed and reverse-transferred to each subject space using the previously created DARTEL template and flow fields. Mean susceptibility values of VOIs were extracted automatically from each co-registered QSM using the REX toolkit (https://web.mit.edu/swg/software.htm).

Visual Assessment of CMB

Two serial QSMs were collected from each patient and anonymized. Two board-certified radiologists (_._, _._, with 12 and 16 years of neuroradiology experience, respectively), blinded to image type (whether 3D-EPI or single-TE GRE QSM) and patient information, independently identified, counted, and anatomically categorized CMB using the Microbleed Anatomical Rating Scale (MARS).[14] CMB were defined as small, round hyperintensities on QSM that could not be followed on consecutive slices like blood

vessels, 2–10 mm in size. Ratings were categorized as no CMB, single CMB, 2–3 CMB, and more than 3 CMB. Care was taken to exclude CMB mimics, including blood vessels, mineralization of deep gray matter nucleus, hemorrhage within the area of infarction, air-bone interface artifacts, partial volume artifacts, and small hemorrhage close to large intracranial hematoma. We used MARS because the agreement in determining the exact location of microbleeds, in addition to its number, is important. We also regard the agreement in diagnosing zero microbleeds important.

Statistical Analysis

Statistical analyses were performed using commercially available software (JMP version 12.0; SAS Institute, Cary, NC). We performed linear regression analyses to assess linearity, as well as the intraclass correlation coefficient (ICC) and Bland-Altman analyses, to determine the agreement between 3 QSMs. Those values were calculated between theoretical and measured susceptibility values in the phantom study and between QSM sequences in the healthy volunteer's study. We also calculated consistency between MR scanners in the phantom study. In the patient study, Cohen κ coefficients were calculated to determine CMB detection agreement between 3D-EPI and GRE QSM (intra-rater agreement), as well as the agreement between raters.

Results

Characteristics of Study Participants

Among 220 patients with CMB who underwent 3D-EPI QSM during the sampling period, we excluded 182 patients with no GRE QSM or with an interval of >1 year between 3D-EPI and GRE QSM. Finally, participants in our study comprised 40 healthy volunteers

(mean age, 59 ± 13 years; 25 women) and 38 patients with CMB (mean age, 51 ± 20 years; 20 women) (Fig. 2). The mean interval between 3D-EPI and GRE QSM scan of CMB patients was 213 days (range, 13–365 days). The characteristics of study participants are listed in Table 1.

Phantom Study

Three QSMs of gadolinium phantoms from each sequence are visualized in Figure 3. Linear regression analysis yielded excellent linearity between measured and theoretical susceptibility values of 3D-EPI QSM on both MR scanners: Skyra, R^2 = 0.996, slope 1.045, P < 0.001; Prisma, R^2 = 0.992, slope 1.133, P < 0.001 (Fig. 4). This finding was further supported by the excellent agreement shown on ICC analysis (Skyra, ICC = 0.997; Prisma, ICC = 0.988) and Bland-Altman analysis (Skyra, mean difference -2 ppb, 95%CI -45 to 40 ppb; Prisma, mean difference 15 ppb, 95%CI -67 to 97 ppb) (Table 2). We also identified very high inter-scanner consistency for 3D-EPI QSM between the Skyra and Prisma scanners (R^2 = 0.984, P < 0.001, ICC = 0.988).

Healthy Volunteer Study

Average normalized QSM images from 3D-EPI, single-TE, and multi-TE GRE depicted contrast consistencies in most VOIs, notably in the paramagnetic regions (Fig. 5). Those comparisons were also appreciated in representative individual QSM images (Fig. 6). The mean susceptibility values of brain regions are shown in Figure 7. No significant difference in mean susceptibility was seen between image sequences for QSM (ANOVA, P = 0.530). We noted excellent linearity between 3D-EPI and GRE QSM (to single-TE GRE, R^2 = 0.981, slope 0.960, P < 0.001; to multi-TE GRE, R^2 = 0.983, slope 0.967, P <

0.001), almost equal to the linearity between single-TE and multi-TE GRE QSM (R^2 = 0.987, slope 0.999, P < 0.001) (Fig. 8a). Bland-Altman plots supported the strong agreement between 3D-EPI and GRE-QSM (to single-TE GRE, mean difference 4 ppb, 95%CI -15 to 23 ppb; to Multi-TE GRE, mean difference 3 ppb, 95%CI -15 to 20 ppb). As a reference, the plot between single-TE and multi-TE GRE QSM showed a mean difference of -1 ppb (95%CI -16 to 14 ppb) (Fig. 8b). ICC calculations showed consistently excellent agreement between 3D-EPI and GRE QSM (to single-TE GRE, ICC = 0.988; to multi-TE GRE, ICC = 0.990). In regional analyses, QSM yielded better consistencies in paramagnetic VOIs (3D-EPI to single-TE GRE, ICC = 0.966; 3D-EPI to multi-TE GRE, ICC = 0.972) than diamagnetic VOIs (3D-EPI to single-TE GRE, ICC = 0.931; 3D-EPI to multi-TE GRE, ICC = 0.944) with the highest agreement depicted in the highly paramagnetic structure of the globus pallidus (Table 3). Among healthy volunteers, physiologic calcifications were apparent in 29 choroid plexuses of the right ventricle and 28 choroid plexuses of the left ventricle. Strong agreements in susceptibility values of choroid plexus calcification were evident between 3D-EPI and GRE QSM (to single-TE GRE, ICC = 0.986; to multi-TE GRE, ICC = 0.965), similar to the agreement between single-TE and multi-TE GRE QSM (ICC = 0.977).

Patient Study

Over 684 brain regions from 38 subjects using 3D-EPI QSM, CMB were identified in 88 locations by Rater A, and in 74 locations by Rater B. Using GRE QSM, CMB were found in 83 locations by Rater A, and in 67 locations by Rater B. The frequency distribution of CMB observed in the patients are provided in Supplemental Digital Content 2 (Supplemental Table 2a and 2b). Representative images of 3D-EPI and GRE QSM in

visualizing CMB are shown in Figure 9. Visual assessment of CMB as depicted by 3D-EPI QSM and GRE QSM exhibited very good intra-rater agreement (Rater A, κ = 0.923, 95%CI 0.876 to 0.970, P < 0.001; Rater B, κ = 0.942, 95%CI 0.905 to 0.979, P < 0.001). Inter-rater agreement was slightly higher for 3D-EPI QSM visual assessment than for GRE-QSM (κ = 0.844, 95%CI 0.786 to 0.904, P < 0.001; κ = 0.819, 95%CI 0.754 to 0.884, P < 0.001, respectively).

Discussion

We assessed the accuracy, reliability, and cerebral microbleeds (CMB) detection performance of 2-min 3-dimensional echo-planar imaging (3D-EPI) quantitative susceptibility mapping (QSM), compared to gradient-recalled echo (GRE) QSM.[15] Gadolinium phantom study yielded excellent linearity between measured and theoretical susceptibilities of 3D-EPI QSM on both MR scanners (Skyra, R^2 = 0.996, P < 0.001; Prisma, R^2 = 0.992, P < 0.001). We also determined a high inter-scanner consistency for 3D-EPI QSM between Skyra and Prisma (R^2 = 0.984, P < 0.001; ICC = 0.988). Excellent linearity was identified between 3D-EPI and GRE QSM (single-TE GRE, R^2 = 0.981; multi-TE GRE, R^2 = 0.983), almost equal to the linearity between single-TE and multi-TE GRE QSM (R^2 = 0.987) in healthy volunteers. Visual assessment of CMB as depicted by 3D-EPI and GRE QSM exhibited almost perfect intra-rater agreement (Rater A, κ = 0.923, P < 0.001; Rater B, κ = 0.942, P < 0.001). The inter-rater agreement of 3D-EPI QSM visual assessment was slightly higher than that of GRE-QSM (κ = 0.844, P < 0.001; κ = 0.819, P < 0.001, respectively).

No prior gadolinium phantom studies of 3D-EPI QSM have been reported, and a previous 3D-EPI QSM study used a simulated phantom without any statistical parameters

of accuracy for comparison.[16] The linear correlation between measured and theoretical susceptibilities of 3D-EPI QSM in our study was equal to the previous study using multi-TE GRE with an Iterative and Deterministic QSM algorithm (R^2 = 0.99).[17] We also noted comparable agreement of 3D-EPI QSM to a previous study using multiple scanners, multi-TE GRE, and MEDI+0 algorithm (ICC 0.99, 95%CI 0.97 to 0.99).[18] Inter-scanner reproducibility was excellent and similar between 3D-EPI and GRE QSM.

Several QSM reproducibility studies on human participants have been conducted, but none described comparisons between 3D-EPI and GRE QSM. They instead compared different field strengths,[19, 20] vendors,[19] sites,[17] and algorithms.[20, 21] Wei et al. used 2D-EPI QSM and demonstrated bias of -5 ppb (95%CI -11 to 20 ppb) with 3D processing, which was improved using their 2D+3D processing to -1 ppb (95%CI -15 to 13 ppb).[21] These values were comparable to the present findings. Further, we obtained higher spatial resolution as an inherent advantage of 3D-EPI QSM. Mean susceptibilities of brain structures in our study were also affirmatory to the postmortem study.[22] The lower consistencies observed in the internal capsule and optic radiation were concordant with the literature, which has stated that the susceptibility of highly oriented white matter structures is affected by anisotropy and microstructure-related phase offsets, precipitating a higher variability.[23, 24] This is further supported by the better consistency we obtained for choroid plexus calcification, which is theoretically less affected by those factors.

CMB evaluation using GRE-QSM was advantageous over T2*-weighted imaging and susceptibility-weighted imaging (SWI), as the method is independent of echo time, thus providing better quantification consistency.[7] As for 3D-EPI QSM, our data showed similar performance to GRE QSM in detecting CMB, as represented by the high intra-rater agreement. Furthermore, we obtained an inter-rater agreement comparable to that of a

past study using SWI and T2*-GRE (ICC, 0.87; ICC, 0.52, respectively).[25] A recent study of single-shot 2D-EPI QSM showed a similar intracerebral hemorrhage area and susceptibility measurement to SWI-QSM (R^2, ranging from 0.93 to 0.98; ICC, ranging from 0.881 to 0.996).[11] However, susceptibility underestimation was evident, notably in the high susceptibility lesion and small hemorrhages (< 100 mm^2). The partial volume effect due to the limited resolution of 2D-EPI was one reason. 3D-EPI, with its higher resolution, may overcome this limitation, thus improving susceptibility estimation, particularly in evaluating small and microhemorrhages.

Our study had several limitations. First, streaking artifacts were seen around the balloon with high susceptibility. To mitigate this effect, we created the ROI in the center of the balloon, sparing the partly affected peripheral region. MEDI+0 automatic zero referencing algorithm has been reported to solve such a problem. However, MEDI+0 is typically used for multi-TE GRE.[18] Air-interface artifacts were also present in the 3D-EPI QSM of some participants, originating from the paranasal sinus and mainly affecting the area of caudate nucleus. It might be one reason for the lower consistencies in caudate nucleus. Second, in the human study, we did not calibrate susceptibility values using normalization reference. Several normalization references have been proposed, including ventricular cerebrospinal fluid (CSF) and white matter structures.[26] Ventricular CSF shows the lowest variability and is unaffected by myelination and anisotropy.[26] However, we found that ventricular CSF often appears heterogeneous, influenced by CSF flow, vessels, and sometimes calcification of the choroid plexus, which could impair reliability. Thus, we did not choose any specific region of interest as a reference, which is equivalent to set the mean susceptibility of the whole brain as the reference in part due to the reference of Larmor frequency. Finally, we excluded a large number of patients with CMB showing

overly long (> 1 year) scan intervals between 3D-EPI and GRE QSM. We were aware that such exclusion might lead to selection bias. However, as the interval increases, the risk of lesion progression would increase, which showed 6% to 23% of increase rates after 2 to 5 years follow up,[27-29] which would undermine the accuracy of evaluations of detection performance.

In conclusion, QSM from 3D-EPI with a clinically favorable shorter acquisition time demonstrated excellent accuracy, reliability, and comparable detection performance to the GRE QSM in patients with cerebral microbleeds, which may foster its clinical use.

REFERENCES

1. Duyn JH, Schenck J. Contributions to magnetic susceptibility of brain tissue. *NMR in Biomedicine.* 2017;30:e3546.

2. Hinoda T, Fushimi Y, Okada T, et al. Quantitative assessment of gadolinium deposition in dentate nucleus using quantitative susceptibility mapping. *Journal of Magnetic Resonance Imaging.* 2017;45:1352-1358.

3. Oshima S, Fushimi Y, Okada T, et al. Brain MRI with Quantitative Susceptibility Mapping: Relationship to CT Attenuation Values. *Radiology.* 2020:182934.

4. Kim H-G, Park S, Rhee HY, et al. Quantitative susceptibility mapping to evaluate the early stage of Alzheimer's disease. *NeuroImage: Clinical.* 2017;16:429-438.

5. Zhang S, Nguyen TD, Rúa SMH, et al. Quantitative susceptibility mapping of time-dependent susceptibility changes in multiple sclerosis lesions. *American Journal of Neuroradiology.* 2019;40:987-993.

6. Chen Q, Chen Y, Zhang Y, et al. Iron deposition in Parkinson's disease by quantitative susceptibility mapping. *BMC neuroscience.* 2019;20:23.

7. Haller S, Vernooij MW, Kuijer JPA, Larsson E-M, Jäger HR, Barkhof F. Cerebral microbleeds: imaging and clinical significance. *Radiology.* 2018;287:11-28.

8. Ciraci S, Gumus K, Doganay S, et al. Diagnosis of intracranial calcification and hemorrhage in pediatric patients: comparison of quantitative susceptibility mapping and phase images of susceptibility-weighted imaging. *Diagnostic and interventional imaging.* 2017;98:707-714.

9. Sati P, Patil S, Inati S, et al. Rapid MR susceptibility imaging of the brain using segmented 3D echo-planar imaging (3D EPI) and its clinical applications. *Magnetom FLASH.* 2017;68:26-32.

10. Sun H, Wilman AH. Quantitative susceptibility mapping using single - shot echo - planar imaging. *Magnetic resonance in medicine.* 2015;73:1932-1938.

11. De A, Sun H, Emery DJ, Butcher KS, Wilman AH. Rapid quantitative susceptibility mapping of intracerebral hemorrhage. *Journal of Magnetic Resonance Imaging.* 2020;51:712-718.

12. Poser BA, Koopmans PJ, Witzel T, Wald LL, Barth M. Three dimensional echo-planar imaging at 7 Tesla. *Neuroimage.* 2010;51:261-266.

13. Olsson E, Wirestam R, Lind E. MRI-Based Quantification of Magnetic Susceptibility in Gel Phantoms: Assessment of Measurement and Calculation Accuracy. *Radiology research and practice.* 2018;2018.

14. Gregoire SM, Chaudhary UJ, Brown MM, et al. The Microbleed Anatomical Rating Scale (MARS): reliability of a tool to map brain microbleeds. *Neurology.* 2009;73:1759-1766.

15. Hagiwara A, Fujita S, Ohno Y, Aoki S. Variability and Standardization of Quantitative Imaging: Monoparametric to Multiparametric Quantification, Radiomics, and Artificial Intelligence. *Invest Radiol.* 2020.

16. Langkammer C, Bredies K, Poser BA, et al. Fast quantitative susceptibility mapping using 3D EPI and total generalized variation. *Neuroimage.* 2015;111:622-630.

17. Lin PY, Chao TC, Wu ML. Quantitative susceptibility mapping of human brain at 3T: a multisite reproducibility study. *American Journal of Neuroradiology.* 2015;36:467-474.

18. Deh K, Kawaji K, Bulk M, et al. Multicenter reproducibility of quantitative susceptibility mapping in a gadolinium phantom using MEDI+ 0 automatic zero referencing. *Magnetic resonance in medicine.* 2019;81:1229-1236.

19. Deh K, Nguyen TD, Eskreis - Winkler S, et al. Reproducibility of quantitative susceptibility mapping in the brain at two field strengths from two vendors. *Journal of magnetic resonance imaging.* 2015;42:1592-1600.

20. Hinoda T, Fushimi Y, Okada T, et al. Quantitative susceptibility mapping at 3 T and 1.5 T: evaluation of consistency and reproducibility. *Investigative radiology.* 2015;50:522-530.

21. Wei H, Zhang Y, Gibbs E, Chen NK, Wang N, Liu C. Joint 2D and 3D phase processing for quantitative susceptibility mapping: application to 2D echo - planar imaging. *NMR in Biomedicine.* 2017;30:e3501.

22. Langkammer C, Schweser F, Krebs N, et al. Quantitative susceptibility mapping (QSM) as a means to measure brain iron? A post mortem validation study. *Neuroimage.* 2012;62:1593-1599.

23. Lancione M, Tosetti M, Donatelli G, Cosottini M, Costagli M. The impact of white matter fiber orientation in single - acquisition quantitative susceptibility mapping. *NMR in Biomedicine.* 2017;30:e3798.

24. Wharton S, Bowtell R. Effects of white matter microstructure on phase and susceptibility maps. *Magnetic resonance in medicine.* 2015;73:1258-1269.

25. Cheng A-L, Batool S, McCreary CR, et al. Susceptibility-weighted imaging is more reliable than T2*-weighted gradient-recalled echo MRI for detecting microbleeds. *Stroke.* 2013;44:2782-2786.

26. Straub S, Schneider TM, Emmerich J, et al. Suitable reference tissues for quantitative susceptibility mapping of the brain. *Magnetic resonance in medicine.* 2017;78:204-214.

27. van Dooren M, Staals J, de Leeuw PW, Kroon AA, Henskens LH, van Oostenbrugge RJ. Progression of brain microbleeds in essential hypertensive patients: a 2-year follow-up study. *American journal of hypertension.* 2014;27:1045-1051.

28. Poels MMF, Ikram MA, van der Lugt A, et al. Incidence of cerebral microbleeds in the general population: the Rotterdam Scan Study. *Stroke.* 2011;42:656-661.

29. Gregoire SM, Brown MM, Kallis C, Jäger HR, Yousry TA, Werring DJ. MRI detection of new microbleeds in patients with ischemic stroke: five-year cohort follow-up study. *Stroke.* 2010;41:184-186.

Table 1: Characteristics of study participants

Characteristic	Value
Healthy volunteers	
No. of volunteers	40
Mean age ± SD (years)	59 ± 13
Sex	
M	15
F	25
Patients	
No. of patients	38
Mean age ± SD (years)	51 ± 20
Sex	
M	18
F	20
Mean interval between QSM (range, days)	213 (13 – 365)
Underlying diseases	
Intracranial neoplasm	15
Cavernoma	9
Aneurysm	8
Other vascular malformation	2
Infarction	2
Inflammatory pseudotumor	1
Microbleeds of unknown etiology	1

Table 2: ICC, R^2, and Bland-Altman analyses between measured and theoretical susceptibility values of gadolinium phantom

QSM Sequence	SKYRA			PRISMA		
	ICC (95%CI)	R^2 (P)	Mean difference (95%CI)	ICC (95%CI)	R^2 (P)	Mean difference (95%CI)
3D-EPI	0.997 (0.987 – 0.999)	0.996 (< 0.001)	-2 ppb (-45 – 40)	0.988 (0.946 - 0.998)	0.992 (< 0.001)	15 ppb (-67 – 97)
Single-TE GRE	0.999 (0.997 – 0.999)	0.999 (< 0.001)	2 ppb (-24 – 20)	0.992 (0.960 - 0.998)	0.991 (< 0.001)	-4 ppb (-77 – 68)
Multi-TE GRE	0.993 (0.964 – 0.999)	0.991 (< 0.001)	5 ppb (-63 – 74)	0.993 (0.964 - 0.999)	0.995 (< 0.001)	-2 ppb (-71 – 66)

Table 3: Regional ICC calculation between QSM sequences

Region	3D-EPI to Single-TE GRE		3D-EPI to Multi-TE GRE		Multi-TE to Single-TE GRE	
	ICC	95%CI	ICC	95%CI	ICC	95% CI
RGP	0.968	0.911 – 0.986	0.980	0.963 – 0.990	0.974	0.947 – 0.987
LGP	0.957	0.896 – 0.980	0.953	0.890 – 0.978	0.979	0.960 – 0.989
RP	0.957	0.910 – 0.978	0.951	0.785 – 0.982	0.969	0.939 – 0.984
LP	0.953	0.897 – 0.977	0.963	0.906 – 0.983	0.977	0.957 – 0.988
RRN	0.806	0.626 – 0.899	0.910	0.835 – 0.952	0.885	0.786 – 0.938
LRN	0.868	0.688 – 0.938	0.891	0.778 – 0.944	0.895	0.811 – 0.943
RSN	0.928	0.858 – 0.963	0.888	0.798 – 0.939	0.915	0.838 – 0.955
LSN	0.864	0.718 – 0.932	0.867	0.745 – 0.931	0.927	0.868 – 0.961
RDN	0.949	0.906 – 0.973	0.945	0.898 – 0.971	0.972	0.948 – 0.985
LDN	0.935	0.841 – 0.970	0.946	0.891 – 0.973	0.973	0.949 – 0.986
RCN	0.791	0.391 – 0.913	0.838	0.652 – 0.920	0.900	0.799 – 0.949
LCN	0.743	0.254 – 0.894	0.822	0.660 – 0.906	0.873	0.650 – 0.944
ROR	0.904	0.826 – 0.948	0.948	0.901 – 0.972	0.919	0.851 – 0.957
LOR	0.913	0.806 – 0.958	0.964	0.934 – 0.981	0.962	0.901 – 0.983
RIC	0.717	0.527 – 0.839	0.749	0.572 – 0.859	0.855	0.744 – 0.920
LIC	0.835	0.702 – 0.911	0.804	0.659 – 0.892	0.831	0.693 – 0.909
SPL	0.819	0.684 – 0.900	0.838	0.714 – 0.910	0.870	0.745 – 0.933
CPC	0.986	0.976 – 0.992	0.965	0.929 – 0.981	0.977	0.945 – 0.989

RGP: right globus pallidus, LGP: left globus pallidus, RP: right putamen, LP: left putamen, RRN: right red nucleus, LRN: left red nucleus, RSN: right substantia nigra, LSN: left substantia nigra, RDN: right dentate nucleus, LDN: left dentate nucleus, RCN: right caudate nucleus, LCN: left caudate nucleus, ROR: right optic radiation, LOR: left optic radiation, RIC: right internal capsule, LIC: left internal capsule, SPL: splenium of corpus callosum, CPC: choroid plexus calcification.

Figure Legends

Figure 1: VOIs from healthy volunteers. VOIs are created semi-automatically based on average normalized QSM images.

Figure 2: Flow diagram for the enrollment of study participants.

Figure 3: QSM of gadolinium phantom: 3D-EPI (a), single-TE GRE (b), and multi-TE GRE (c) with gradually increased concentrations. ROIs are created as circular regions in the center of the balloon to minimize the effect of adjacent streaking artifacts, with a control ROI placed in the water region (d). Gadolinium concentrations of each phantom was as follows: 0.25 (red), 0.5 (green), 0.75 (blue), 1.0 (yellow), 1.5 (light blue), 2.0 (orange), and 2.5 mmol/L (brown). An ROI was also placed on the water (purple, surrounding water).

Figure 4: Measured and theoretical susceptibility values of three QSMs are shown. The regression line between the measured and theoretical value of 3D-EPI QSM shows excellent linearity. Corresponding values of GRE QSMs (single-TE and multi-TE) are also equivalent. Upper row: Skyra; lower row: Prisma.

Figure 5: Comparison of average QSMs among all volunteers generated from 3D-EPI, single-TE GRE, and multi-TE GRE on the same slice. The intensities of most brain structures are visually consistent.

Figure 6: Representative individual QSM images from healthy volunteers. Individual QSM generated from 3D-EPI, single-TE GRE, and multi-TE GRE on the same slice.

Figure 7: Mean susceptibility values of VOIs are comparable between the 3 QSM sequences. No significant difference in mean susceptibility was seen between image sequences for QSM (ANOVA, $P = 0.530$). RGP: right globus pallidus, LGP: left globus pallidus, RRN: right red nucleus, LRN: left red nucleus, RSN: right substantia nigra, LSN: left substantia nigra, RP: right putamen, LP: left putamen, RDN: right dentate nucleus, LDN: left dentate nucleus, RCN: right caudate nucleus, LCN: left caudate nucleus, SPL: splenium of corpus callosum, ROR: right optic radiation, LOR: left optic radiation, RIC: right internal capsule, LIC: left internal capsule.

Figure 8: Scatter plots and Bland-Altman plots of healthy volunteers. (a) The regression line of 3D-EPI QSM in the study of healthy volunteers also demonstrates excellent linearity, approaching the linearity between GRE QSMs. (b) Low estimated biases are depicted in Bland-Altman plots (to single-TE GRE, mean difference 4 ppb, 95%CI -15 to 23 ppb; to multi-TE GRE, mean difference 3 ppb, 95%CI -15 to 20 ppb), reflecting the low probability of systematic error. As a reference, the plot between single-TE and multi-TE GRE QSM showed a mean difference of -1 ppb (95%CI -16 to 14 ppb). Several outliers are present, but the proportion is considerably small compared to the 680 measurement points in total.

Figure 9: Representative images of patients with cerebral microbleeds. 3D-EPI QSM (a-c) and GRE-QSM (d-f) are shown. 3D- EPI and GRE were obtained on two different days. Each paired image is obtained from different patients, showing paramagnetic spots

suggesting microbleeds in the left parietal lobe (a, d), right putamen (b, e), and cerebellum (c, f). These microbleeds are visually equivalent on both 3D-EPI QSM and GRE-QSM.

Supplemental Figure 1: Outline of QSM reconstruction. (a) Raw-phase image (unfiltered) from 3D-EPI or GRE acquisition. (b) Result of the Laplacian-based phase unwrapping. (c) Corresponding magnitude image was used for creating (d) brain mask by using BET. (e) Tissue phase map as the result of background phase removal (V-SHARP), of which furtherly processed using the iLSQR algorithm to create (f) QSM.

Fig. 1

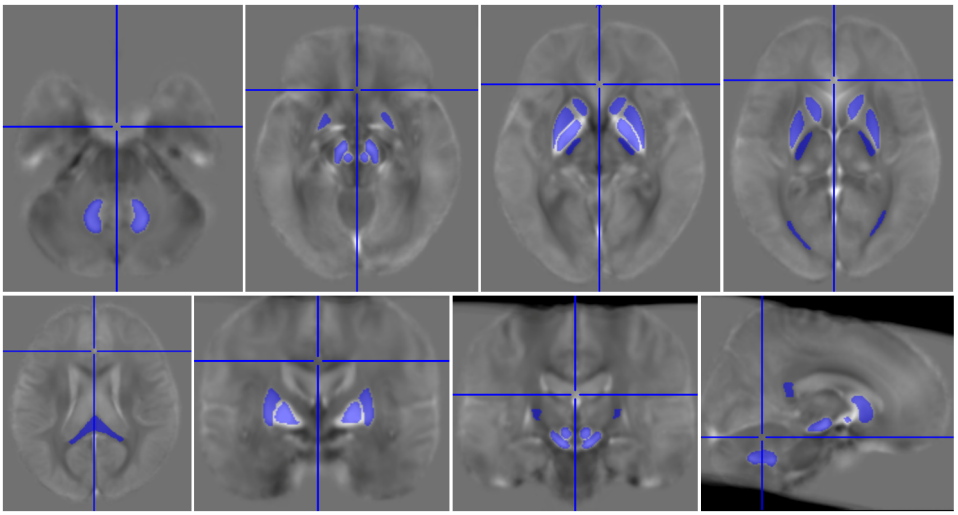

Fig. 2

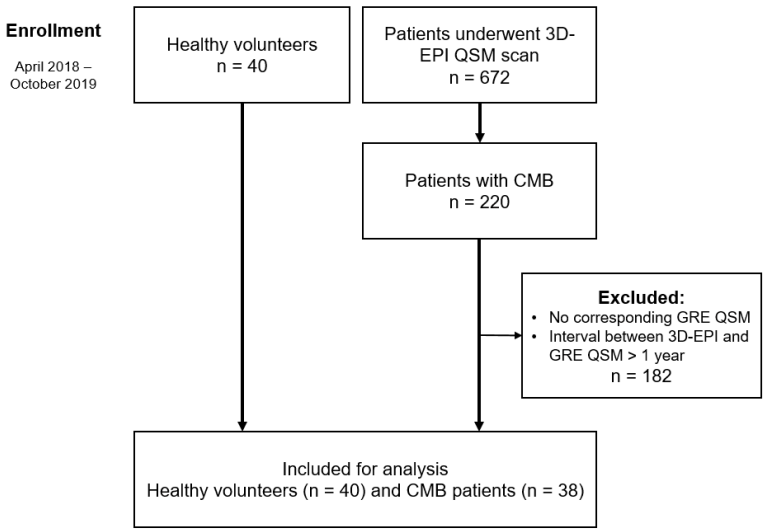

Fig. 3

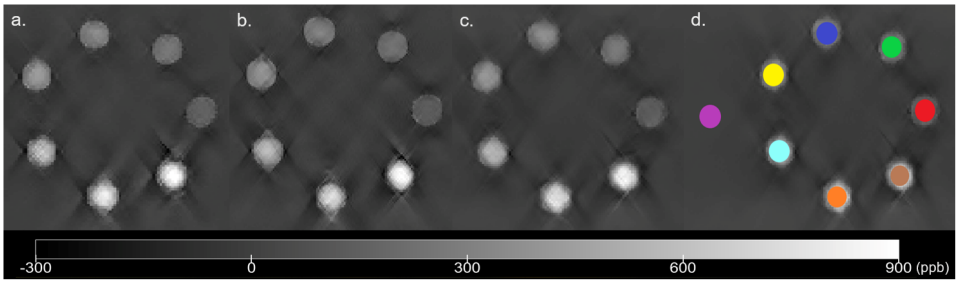

Fig. 4

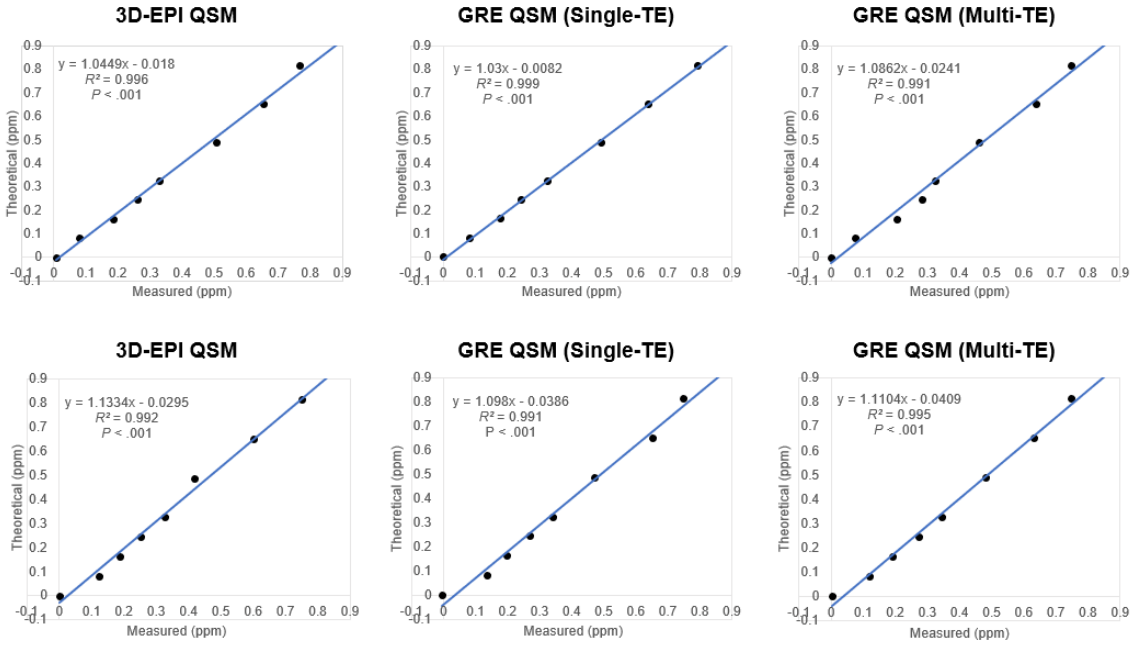
3D-EPI QSM
y = 1.0449x - 0.018
R² = 0.996
P < .001
GRE QSM (Single-TE)
y = 1.03x - 0.0082
R² = 0.999
P < .001
GRE QSM (Multi-TE)
y = 1.0862x - 0.0241
R² = 0.991
P < .001
3D-EPI QSM
y = 1.1334x - 0.0295
R² = 0.992
P < .001
GRE QSM (Single-TE)
y = 1.098x - 0.0386
R² = 0.991
P < .001
GRE QSM (Multi-TE)
y = 1.1104x - 0.0409
R² = 0.995
P < .001
Theoretical (ppm)
Measured (ppm)

Fig. 5

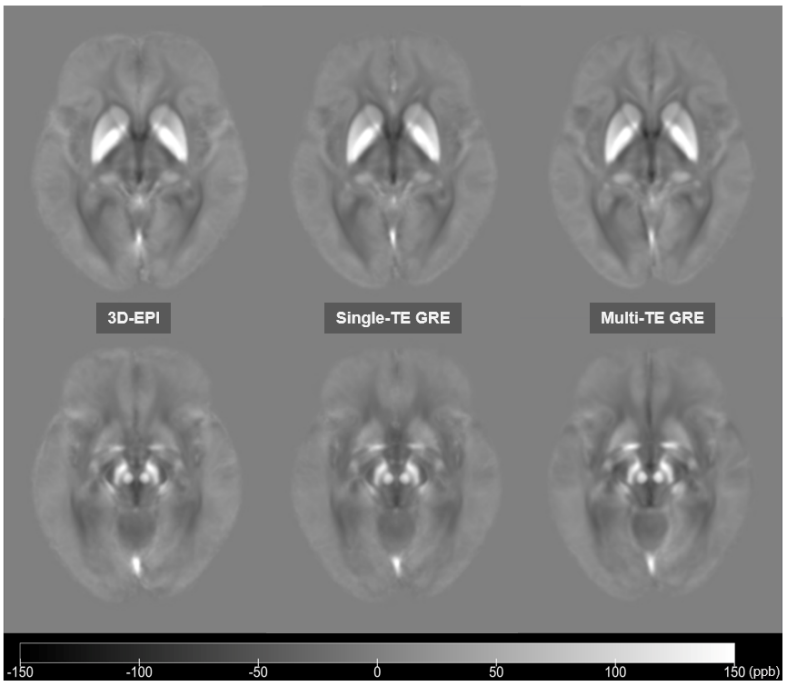
3D-EPI
Single-TE GRE
Multi-TE GRE
-150
-100
-50
0
50
100
150 (ppb)

Fig.6

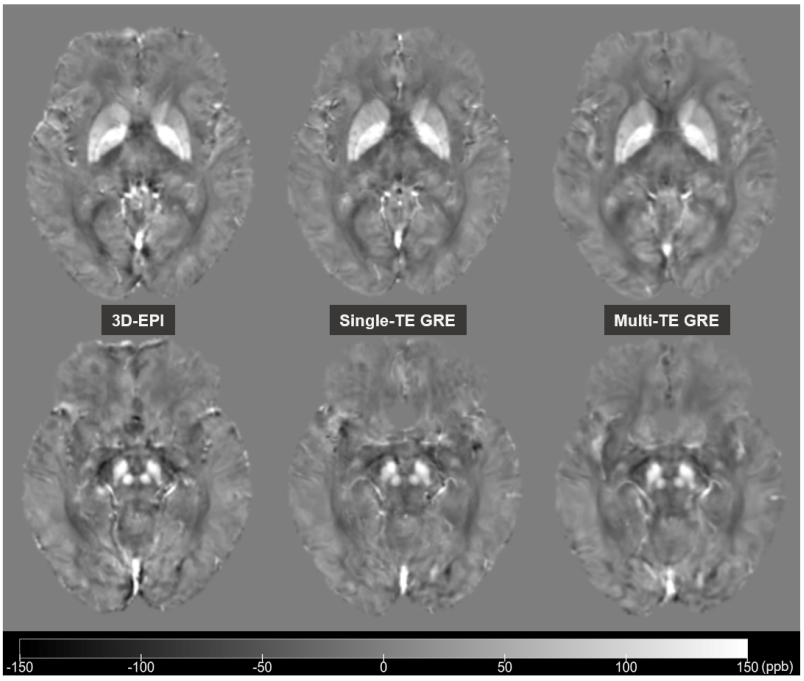
3D-EPI
Single-TE GRE
Multi-TE GRE
-150
-100
-50
0
50
100
150 (ppb)

Fig. 7

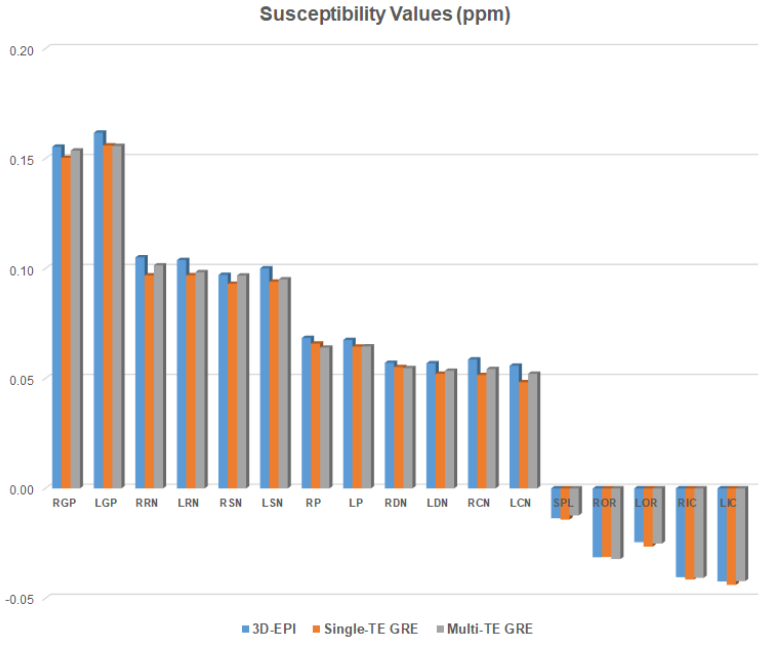
Susceptibility Values (ppm)
0.20
0.15
0.10
0.05
0.00
-0.05
RGP
LGP
RRN
LRN
RSN
LSN
RP
LP
RDN
LDN
RCN
LCN
SPL
ROR
LOR
RIC
LIC
3D-EPI
Single-TE GRE
Multi-TE GRE

Fig. 8

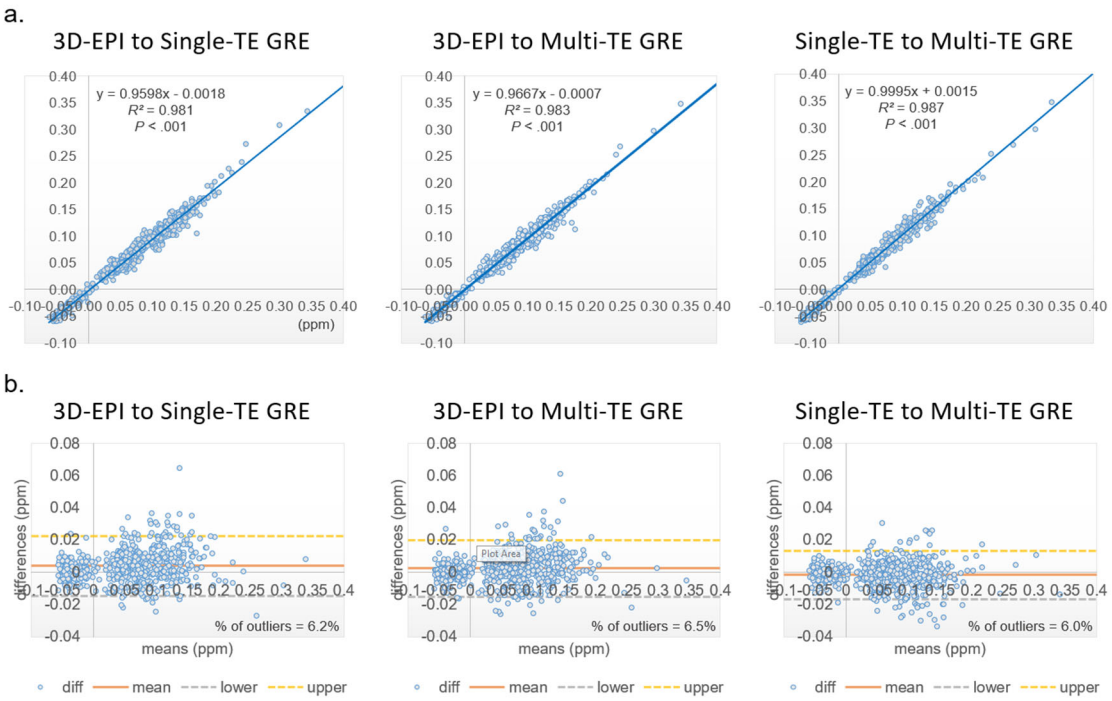
a.
3D-EPI to Single-TE GRE
y = 0.9598x - 0.0018
R² = 0.981
P < .001
3D-EPI to Multi-TE GRE
y = 0.9667x - 0.0007
R² = 0.983
P < .001
Single-TE to Multi-TE GRE
y = 0.9995x + 0.0015
R² = 0.987
P < .001
(ppm)
b.
3D-EPI to Single-TE GRE
3D-EPI to Multi-TE GRE
Single-TE to Multi-TE GRE
differences (ppm)
means (ppm)
% of outliers = 6.2%
% of outliers = 6.5%
% of outliers = 6.0%
diff
mean
lower
upper

Fig. 9

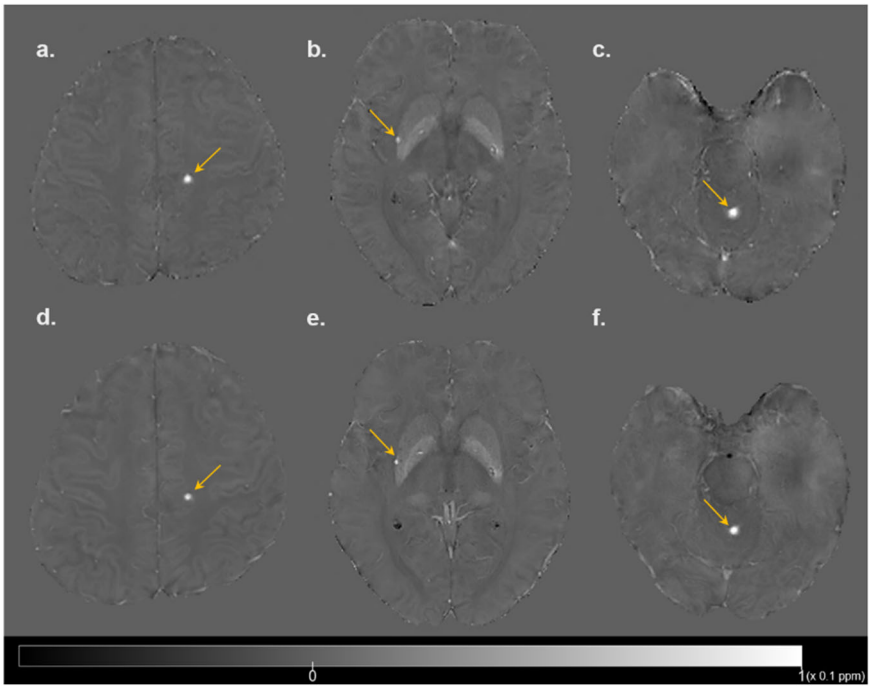
a.
b.
c.
d.
e.
f.
0
1(x 0.1 ppm)